Journal of Materials Chemistry A

ROYAL SOCIETY OF CHEMISTRY

PAPER

View Article Online
View Journal

Cite this: DOI: 10.1039/d5ta02041g

Easily accessible 3D flow fields through 3D-patterned GDL to enhance PEMFC performance *via* excellent water–gas separation transport†

Xi Cheng,[ab] Can He,[b] Qinglin Wen,[b] Yuzhuo Jiang,[b] Wei Li,[b] Jiahao Huang,[ab] Wentao Huang,[b] Xingyu Zhu,[b] Xueyan Chu,[b] Fandi Ning,[b] Lining Sun,[a] Bin Tian[b] and Xiaochun Zhou *[bc]

Proton exchange membrane fuel cells (PEMFCs) are considered highly efficient energy conversion devices utilizing sustainable green energy. However, commonly occurring water flooding and inefficient mass transfer at high current densities significantly restrict the advancement of higher power density due to obstructed electrochemical reactions. Herein, we developed a readily available three-dimensional (3D) flow field by assembling a regularly 3D-patterned gas diffusion layer (GDL) with a conventional bipolar plate to overcome these challenges. The 3D-patterned GDL with ribs and channels was prepared by multi-step vacuum filtration using a specialized mold. The channels in the 3D-patterned GDL provided independent shortcuts for water drainage, while the channels in the conventional bipolar plate offered independent pathways for air, facilitating clear separation between water and gas transport. Consequently, the 3D flow field effectively prevented water flooding and demonstrated exceptional humidity tolerance under varying air supply conditions. Moreover, it exhibited a lower pressure drop and achieved a high peak power density of 1.7 W cm^{-2}. Under a low air stoichiometric ratio of 1.5, it showed a 73% improvement in performance compared to the conventional flow field, with only a 5% fluctuation under wide humidity conditions. Given its easy availability, the new 3D flow field, combining a 3D-patterned GDL with a conventional bipolar plate, presents an unprecedented concept in 3D flow field design and demonstrates considerable potential for the development of ultra-high-performance fuel cells.

Received 12th March 2025
Accepted 16th April 2025

DOI: 10.1039/d5ta02041g

rsc.li/materials-a

1 Introduction

Proton exchange membrane fuel cells (PEMFCs), powered by hydrogen,[1–3] are attracting considerable attention and show great potential in clean energy applications.[4,5] Enhancing the power density of PEMFCs is crucial for their continued development.[6] However, power density is strongly limited by mass transfer between the flow field and catalyst layer.[7,8] At the cathode, a substantial oxygen supply is required at high power densities (*i.e.*, high current density)[9,10] for efficient electrochemical reactions. High current density leads to considerable water production. A certain amount of water is necessary to maintain the optimal proton conductivity of the membrane.[11] However, excessive water can cover the catalyst layer, hindering the reaction, and accumulate in the gas diffusion layers (GDLs) and flow field, obstructing oxygen transfer if not managed effectively.[12,13]

To accelerate mass transfer, diverse flow fields and GDLs have been designed and optimized.[14] Conventional flow field structures, such as parallel,[15] serpentine,[15,16] and interdigitated,[17,18] are relatively simple to fabricate but suffer from uneven gas distribution or limited water drainage.[19] Advanced structures like biomimetic flow fields, inspired by natural forms, such as leaf-shaped,[20] fin-like,[21] wavy (Scheme 1a and b),[22] and alveolar structures,[23] have been explored to promote more rapid gas transfer and enhanced performance. Furthermore, incorporating baffles into flow channels to create three-dimensional (3D) flow fields has proven to be an effective modification.[24,25] Baffles drive gas flow to change direction, promoting forced convection and enhancing longitudinal mass transfer to the catalyst layer.[26] They also increase local gas velocity, facilitating water removal.[27] The 3D fine mesh flow field developed by Toyota Mirai has significantly improved fuel cell stack performance and lifespan through efficient mass transfer and superior water management.[28] However, these advanced 3D flow fields face considerable challenges, including high

[a]Department of Chemistry, College of Sciences, Shanghai University, Shanghai, 200444, China

[b]Advanced Materials Division, Suzhou Institute of Nano-Tech and Nano-Bionics, Chinese Academy of Sciences (CAS), Suzhou, 215123, China

[c]Key Laboratory of Precision and Intelligent Chemistry, University of Science and Technology of China, Hefei, 230026, China

† Electronic supplementary information (ESI) available. See DOI: https://doi.org/10.1039/d5ta02041g

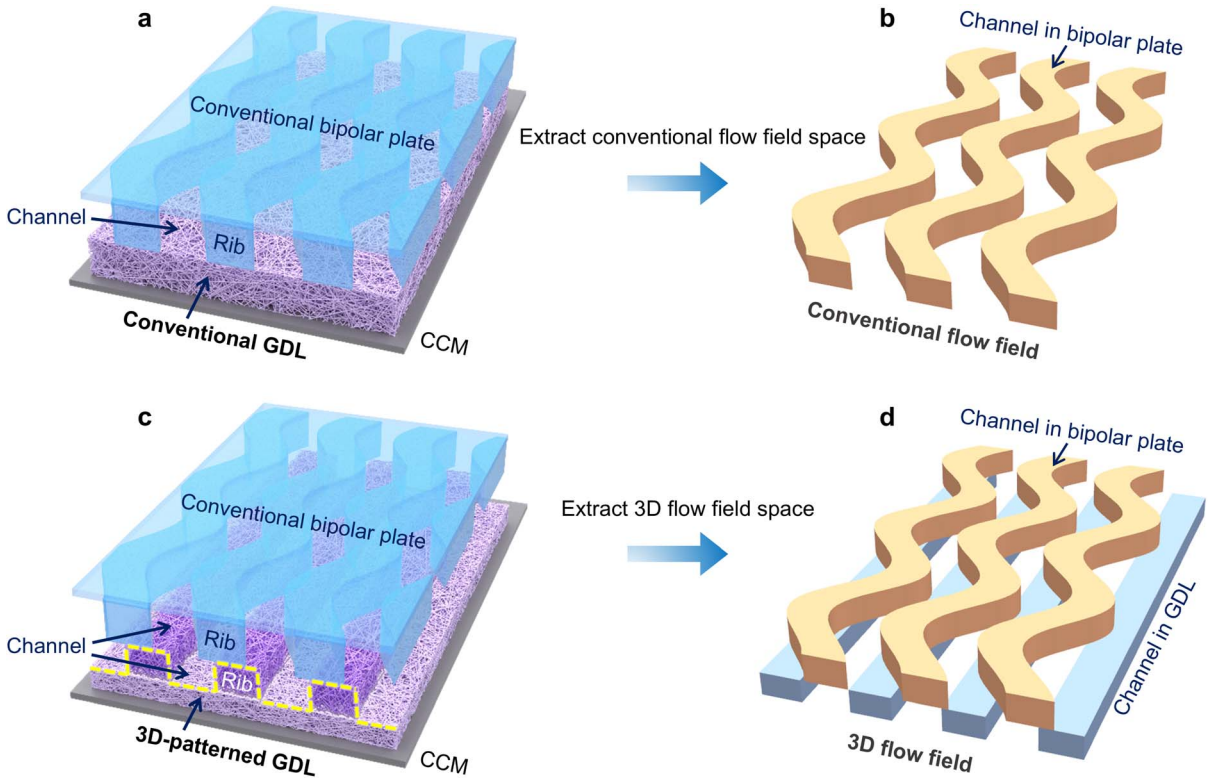

Scheme 1 Schematic of the conventional flow field and 3D flow field used in this work. (a) Fuel cell structure with a conventional flow field, composed of a conventional GDL and a conventional waveform bipolar plate. A catalyst-coated membrane (CCM) is also included. (b) Extracted structure of the conventional flow field. (c) Fuel cell structure with the novel 3D flow field, composed of a 3D-patterned GDL and a conventional waveform bipolar plate. (d) Extracted structure of the 3D flow field.

manufacturing costs and limited practical application, and remain primarily at the theoretical simulation stage.[29]

GDL is a critical component in PEMFCs and strongly affects the mass transfer between the flow field and catalyst layer. Early studies revealed inefficient mass transfer due to the homogeneous structure of the GDL, with flat surfaces on both sides (Scheme 1a and b).[30] To mitigate water flooding, multi-layer GDLs with gradient porosity and wettability were developed, enhancing drainage efficiency through capillary forces between the layers.[31–33] Nevertheless, the sharing transport pathways of water and gas in the GDL may lead to severe mass transfer losses when liquid water blocks the gas channels. Therefore, it is necessary to construct dedicated channels for water management. Hydrophilic substances,[34] pore-forming agents,[35] regular hydrophilic patterns,[36] holes and slits[37,38] were introduced into GDLs to create specific water removal pathways. These pathways separate water and gas to a certain extent, alleviating water flooding at high current densities and improving fuel cell performance effectively.[39] However, the conventional flat structure of GDL remains unchanged, and dead or low-velocity zones beneath the ribs persist, limiting the mass transfer and performance improvement in PEMFCs.[40]

Herein, we developed a novel 3D flow field that is easily available through a regularly 3D-patterned GDL and a conventional waveform bipolar plate (Scheme 1c). The use of conventional bipolar plates effectively avoids fabrication complexities and additional cost burdens. Compared to the conventional flow field (Scheme 1b), the 3D flow field incorporates additional flow channels provided by the 3D-patterned GDL (Scheme 1d). Notably, the 3D flow field facilitates highly efficient water–gas separation, enabling independent water removal and gas transport without dead zones beneath the ribs. It exhibits a much lower pressure drop than a conventional flow field, reducing gas transport resistance and losses. With superior mass transfer and water management, the 3D flow field achieves high PEMFC performance and wide humidity tolerance. Consequently, this novel 3D flow field design provides a promising solution for fuel cells, redox flow batteries,[41,42] and other energy storage and conversion devices.

2 Results and discussion

2.1 Construction and characterization of the 3D flow field

The regularly 3D-patterned GDL is a key component of the new 3D flow field. The preparation of the GDL, shown in Fig. 1a, involves four main steps through a layer-by-layer vacuum filtration method. First, a microporous layer (MPL) is formed by filtering a mixed slurry of carbon materials and polytetrafluoroethylene (PTFE) onto a filter membrane (Fig. 1a1). Second, a mixed slurry is filtered onto the MPL to prepare the support layer (Fig. 1a2), which provides structural support for MPL and the subsequent layer. Third, a 3D-printed mold is used

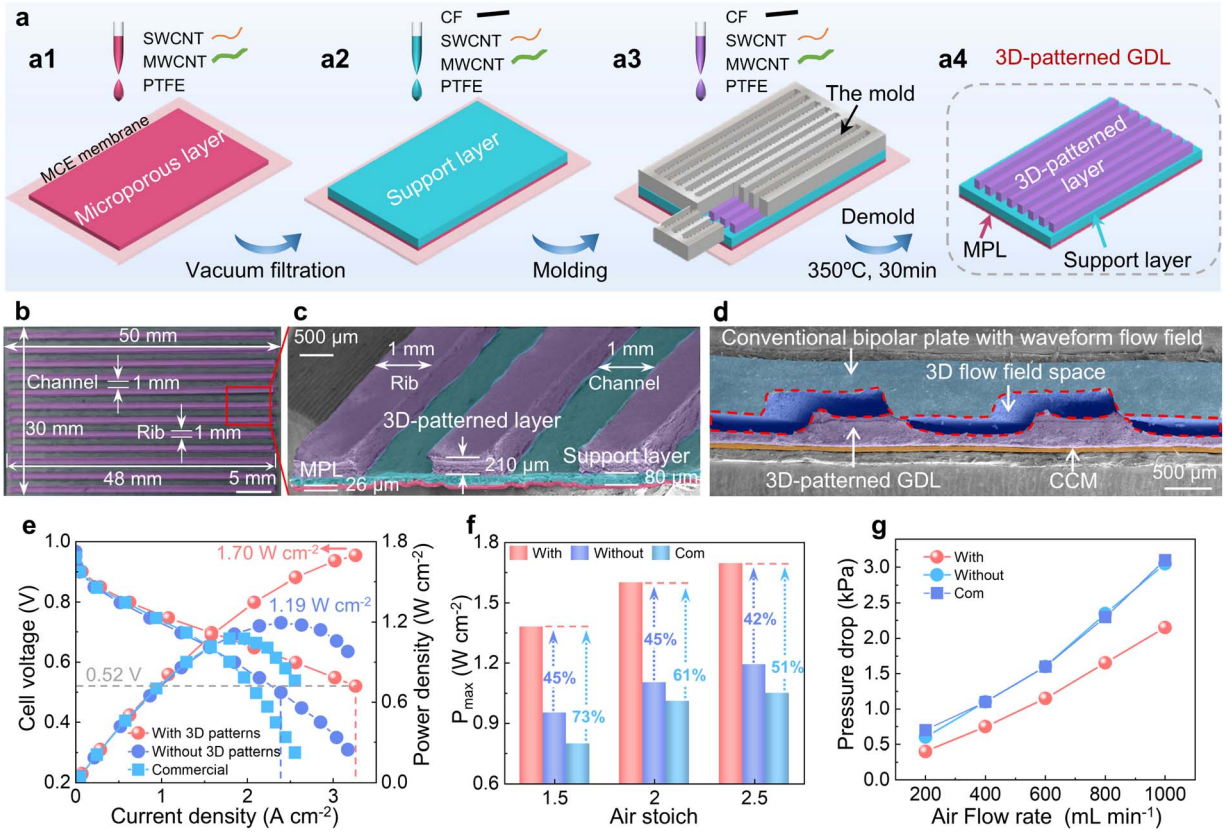

Fig. 1 Preparation and characterization of the 3D flow field. (a) Preparation process of the 3D-patterned GDL. (b) Optical image of the 3D-patterned GDL. (c) Cross-sectional SEM image of the 3D-patterned GDL. (d) Cross-sectional SEM image of the 3D flow field. (e) Fuel cell performance of the 3D flow field and conventional flow fields (including our GDL without the 3D-patterned layer and a commercial GDL). The fuel cells were tested under the following conditions: 80 °C, 100 kPa_{gauge} back pressure, and 60% RH for both anode and cathode under hydrogen-air conditions. (f) Comparison of peak power density at different air stoichiometric ratios. (g) Pressure drops.

as a mask to partially cover the support layer during filtration of the mixed slurry to obtain a 3D-patterned layer (Fig. 1a3). Finally, the 3D-patterned GDL is removed from the filter membrane, and treated at 350 °C for 30 minutes (Fig. 1a4).

Fig. 1b displays a 3D-patterned GDL with dimensions of 50 mm in length and 30 mm in width. The straight parallel patterns span 48 mm in length, and the ribs and channels formed by the 3D patterns are both 1 mm in width. The 3D-patterned GDL consists of three functional layers: an MPL of approximately 26 μm, a support layer of about 80 μm, and a 3D-patterned layer of around 210 μm in thickness, as shown in Fig. 1c and S2.† Each layer is embedded with sufficient PTFE and exhibits hydrophobic nature (contact angle > 146°, Fig. S3†). Fig. 1d shows the detailed structure of the 3D flow field composed of a 3D-patterned GDL (coloured purple) and a conventional bipolar plate with a waveform flow field (coloured light blue). The channels on the bipolar plate and channels on the 3D-patterned GDL together provide flow pathways for gas and water in three dimensions as coloured dark blue, while the conventional 2D flow fields (Fig. S5c†) force air and water to share identical channels, preventing the effective water–gas separated transport. Additionally, the compression under the bipolar plate ribs often creates low-velocity or dead mass transfer zones, thereby impeding air transport and increasing the risk of flooding. The 3D flow field provides three-dimensional flow directions, which is conducive to uniform gas distribution and reduces the accumulation of liquid water beneath the ribs of bipolar plates. More excitingly, unlike the complex three-dimensional flow fields found on bipolar plates, this 3D flow field consists of components with simple patterns, making it easier to prepare and control.

The 3D flow field greatly enhances mass transfer in PEMFCs, particularly at high current densities. As shown in Fig. 1e, the 3D flow field exhibits minimal concentration polarization even at current densities exceeding 3 A cm^{-2} under an air stoichiometric ratio of 2.5. Conversely, the conventional flow fields experience significant concentration polarization, with a rapid voltage drop occurring as the current density approaches 1.5 A cm^{-2}. The GDLs prepared without 3D patterns and commercial GDL exhibit peak power densities of 1.19 W cm^{-2} and 1.13 W cm^{-2}, respectively, both substantially lower than that of 3D-patterned GDL (1.70 W cm^{-2}). Remarkably, the 3D-patterned GDL consistently demonstrates outstanding mass transfer and more pronounced performance improvement as the air stoichiometric ratio decreases (Fig. 1f). At an air stoichiometric ratio as low as 1.5, the 3D flow field maintains a peak power

density of 1.38 W cm^{-2}, which is 73% and 45% higher than the 0.80 W cm^{-2} and 0.95 W cm^{-2} of the conventional flow field formed by commercial GDL and GDL without 3D patterns (Fig. S7a†). Therefore, the 3D-patterned layer plays a dominant role in enhancing the PEMFC performance.

Electrochemical impedance spectroscopy (EIS) (Fig. S8†) further proves the reduced mass transfer impedance caused by the 3D structure. Without the 3D-patterned layer, the GDL composed exclusively of an MPL and a support layer shows the mass transfer resistance (R_{mt}) of 338 mohm cm^2, which is much higher than that of the 3D flow field (109 mohm cm^2). Compared with the commercial GDL, the R_{mt} of 3D-patterned GDL also decreases by 69% and 70% at air stoichiometric ratios of 1.5 and 2.5, respectively, exhibiting efficient mass transfer in the 3D flow field. Notably, the 3D flow field balances high mass transfer efficiency with a low pressure drop. Given the similar flat structures of GDL without the 3D patterns and commercial GDL, the 3D flow field cannot be constructed, thereby resulting in higher pressure drops than GDL with a 3D-patterned configuration (Fig. 1g). At different air flow rates, the 3D flow field consistently exhibits lower pressure drop, reducing air transfer resistance and promoting uniform reactant distribution,[43] which may enhance its competitiveness in practical applications.

2.2 Optimal channel depth in 3D-patterned GDL

The depth of channels plays a critical role in mass transfer. The effects of channel depth on PEMFC performance were investigated by varying the mass loading of all components in the 3D-patterned layer. As shown in Fig. 2a and S20,† when the mass loading is increased from 0 mg cm^{-2} to 8 mg cm^{-2}, the channel depth correspondingly rises from 0 μm to 269 μm. First, deeper flow channels provide more space for gas and water, thereby enhancing transfer efficiency and preventing water flooding. However, excessive mass transfer may result in detrimental effects like dehydration of the proton exchange membrane (PEM). Second, increased channel depth correlates with a thicker GDL, potentially reducing its gas permeability.

Fuel cell performance of 3D flow fields with increasing depths under different air stoichiometric ratios exhibits a volcanic trend in Fig. 2b, c and S21a–c.† The power density at 0.6 V (Fig. 2b) and current density at 0.5 V (Fig. 2c) gradually increase when the mass loading rises from 0 mg cm^{-2} to 6 mg cm^{-2}. This improvement can be attributed to reduced mass transfer impedance resulting from deeper channels in the GDL. However, a further increase in channel depth causes a significant drop in performance. The 3D-patterned layer with a mass loading of 6 mg cm^{-2} (about 212 μm) is determined to be the optimal channel depth in 3D-patterned GDL.

The dual effects of flow channel depth on the PEMFC performance are further demonstrated through EIS. On the one hand, deeper channels facilitate low airflow resistance. As shown in Fig. 2d and S21d,† a progressive increase in depth results in a marked decrease in R_{mt}. Meanwhile, airflow slows down in deeper channels, leading to a reduced pressure drop (Fig. S22c†). On the other hand, overly deep channels can lead to higher electronic resistance and insufficient contact with bipolar plates and the catalyst layer. The ohmic resistance (R_s) remains relatively unchanged at approximately 42.5 mohm cm^2 at first, followed by an increase when the mass loading exceeds 6 mg cm^{-2} (Fig. 2d). It can be attributed to the dehydrated PEM, the contact resistance and the longer electron transfer pathway. The charge transfer resistance (R_{ct}) also generally exhibits an increasing trend with the deeper 3D channel depth due to the incomplete three-phase interface and inefficient proton and electron supply in the MPL/catalyst interface. Additionally, the thickened GDLs cause unfavorable gas permeation. There is a plummet of gas flux coefficient when coming to 7 mg cm^{-2} (Fig. S22b†), ultimately decreasing the gas transport efficiency from the bipolar plate to the catalyst layer.

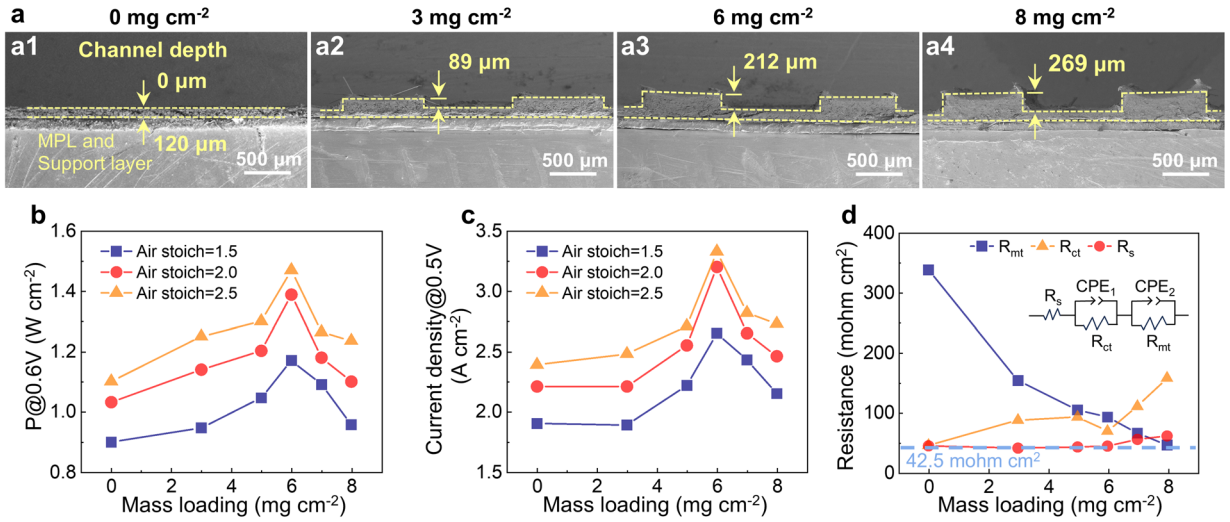

Fig. 2 Effects of channel depth on fuel cell performance. (a) Cross-sectional SEM images of patterned GDL with different channel depths. (b) Power density at 0.6 V under different air stoichiometric ratios. (c) Current density at 0.5 V under different air stoichiometric ratios. (d) EIS fitting results of mass transfer resistance (R_{mt}), charge transfer resistance (R_{ct}), and ohmic resistance (R_s).

2.3 Optimal channel width and shape in 3D-patterned GDL

The distinct configuration of the 3D flow field is also a critical factor in mass transfer. We investigate its optimal structure from two aspects: channel width and shape in the 3D-patterned GDL. First, as shown in Fig. 3a, a conventional waveform bipolar plate, which has been proven to be the most effective structure in enhancing mass transfer[44] (Fig. 3a1), is matched with the parallel patterned-GDL of different channel widths, including 0.5 mm, 1.0 mm, 1.5 mm, and 2.0 mm (Fig. 3a2–a5). Wider flow channels provide more space for gas transport but simultaneously lower the flow velocity and decrease the gas-catalyst effective contact area. Second, based on the compatibility of the waveform-parallel configuration, a conventional parallel bipolar plate (Fig. 3b1) is matched with the wavy patterned GDL (Fig. 3b2) to construct a 3D flow field. Optical images of the five GDLs are shown in Fig. S23.†

Narrow channels are favorable to PEMFC performance, and the parallel-patterned GDL featuring a 1.0 mm channel exhibits the highest peak power density of 1.70 W cm^{-2} (Fig. 3c, S24a and b†). A slight performance degradation is observed for the 0.5 mm channel compared to the 1.0 mm (Fig. 3d–e), with power density at 0.6 V (1.42 W cm^{-2} *vs.* 1.47 W cm^{-2}) and current density at 0.5 V (3.17 A cm^{-2} *vs.* 3.35 A cm^{-2}). The narrower channel contributes to mass transfer by increasing the gas flow velocity and facilitating water removal. However, the performance decline may be attributed to poor compatibility with the bipolar plate in channel width. As the channel width exceeds 1.0 mm, there is a considerable drop in performance due to the poor mass transfer in wider channels.

Moreover, the 3D flow field formed by the wavy-patterned GDL and parallel bipolar plate exhibits inefficient mass transfer, with a 10% decline in power density at 0.6 V (1.32 W cm^{-2}) and 12% decrease in current density at 0.5 V (2.95 A cm^{-2}). This is primarily attributed to restricted air transport in the parallel channels provided by bipolar plates and prolonged water drainage pathways along the wavy channels provided by the

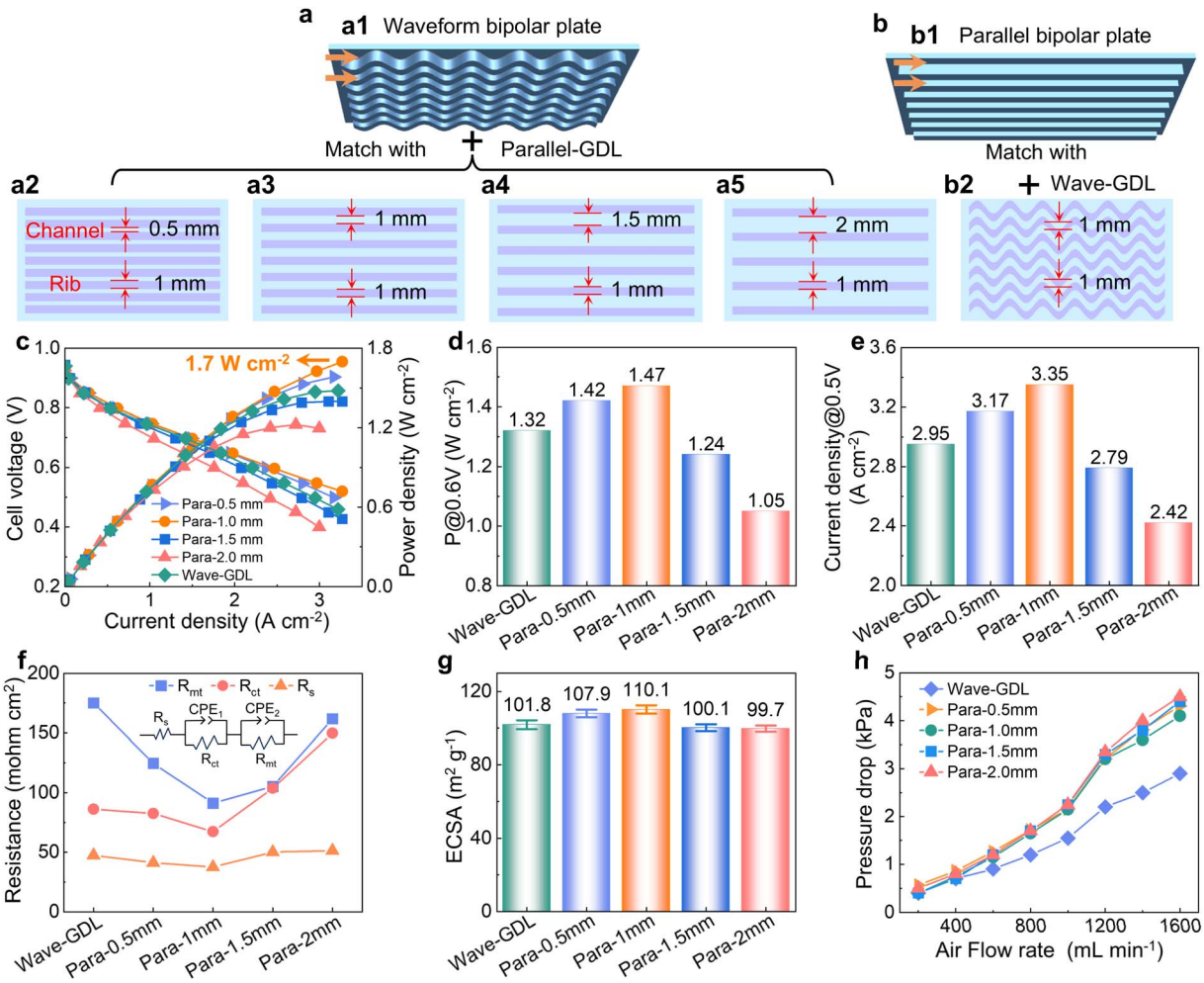

Fig. 3 Effects of 3D flow field types with different channel widths and shapes of 3D-patterned GDL on fuel cell performance. (a) Waveform bipolar plate matched with parallel 3D-patterned GDL of different channel widths, including 0.5 mm (a2), 1.0 mm (a3), 1.5 mm (a4), and 2.0 mm (a5). (b) Parallel bipolar plate matched with wavy 3D-patterned GDL. (c) Polarization curves of different 3D flow field types under an air stoichiometric ratio of 2.5. (d) Comparison of power density at 0.6 V. (e) Comparison of current density at 0.5 V. (f) Fitting results of mass transfer resistance (R_{mt}), charge transfer resistance (R_{ct}), and ohmic resistance (R_s). (g) ECSA. (h) Pressure drops.

GDL. Additionally, the polarization curves of 3D-patterned GDLs matched with the interdigital and serpentine bipolar plates are shown in Fig. S24e–h.† The GDLs substantially enhance the performance across various bipolar plate configurations, with the 3D flow field of waveform bipolar plate-parallel pattern GDL achieving the best performance.

EIS further reveals the lowest impedances of parallel-patterned GDL with 1.0 mm channels (Fig. 3f and S24c†). Despite narrow channels being generally beneficial for efficient mass transfer, the GDL with 0.5 mm channels exhibits a higher R_{mt} (125 mohm cm^2) than that of 1.0 mm channels (91 mohm cm^2) due to the incompatibility with conventional flow channels. The slight increase in R_{ct} and R_s resulted from the inefficient mass transfer. Wide flow channels are unfavorable to both mass and electron transfer. As the channel width increases to 2.0 mm, R_{mt} is 78% higher and R_s is 37% higher relative to the 1.0 mm channels. The increased ohmic resistance indirectly contributes to the elevated R_{ct} by limiting the electron supply, thereby slowing the electrochemical reactions. For the 3D flow field formed by the wavy-patterned GDL and parallel bipolar plate, the performance decline is primarily caused by the high R_{mt} of 175 mohm cm^2 associated with poor air transport in the parallel bipolar plate and slow water removal in the sinuous channels of the wavy-patterned GDL.

The GDL with narrow, parallel channels exhibits a high ECSA (Fig. S24d† and 3g). With identical CCM and MPL, the GDL with 1.0 mm channels demonstrates a higher ECSA (110.1 $\pm$ 2.3 m^2 g^{-1}) compared to wavy-patterned GDL (101.8 $\pm$ 2.5 m^2 g^{-1}) due to more adequate reactants delivered to the catalyst layer, thereby resulting in higher electrochemical reaction rates. Among the straight channels, the ECSA of 0.5 mm channels is slightly lower than that of 1.0 mm, primarily attributed to the inefficient mass transfer. Moreover, the much lower ECSA of 1.5 mm and 2 mm channels result from the reduced contact between the gas and the catalyst, which considerably diminishes the reaction efficiency.

The pressure drop in a 3D flow field is primarily governed by the design of bipolar plates and does not directly correlate with the higher PEMFC power density. As shown in Fig. 3h, the 3D flow field constructed by the wavy-patterned GDL and parallel bipolar plate exhibits the lowest pressure drop, which is attributed to the low air transport resistance in the straight channels. However, the excessively low pressure drop fails to provide a sufficient driving force for water discharge in the flow field. Additionally, for the same bipolar plate, changes in the channel width in GDL show minimal effects on the pressure drop. Subtle differences begin to emerge only when the airflow exceeds 1200 mL min^{-1}. Among the different channel widths, the 1.0 mm channel exhibits the lowest pressure drop.

2.4 Excellent mass transfer over wide operating conditions and stability of the 3D flow field

The diverse applications of PEMFCs expose them to complex and varying environmental conditions. Therefore, it is essential for PEMFCs to maintain excellent and stable mass transfer performance across diverse operating conditions. Herein, we investigated the mass transfer of the 3D flow field through different humidity levels and back pressures.

The 3D flow field demonstrates stable, high-performance operation in a wide humidity range. In the range of 30% RH to 100% RH, humidity has a negligible influence on the polarization curves of the 3D flow field (Fig. 4a). As shown in Fig. 4b, the power density at 0.6 V fluctuates by only 5%, indicating efficient water management of the 3D flow field. Although the conventional flow field exhibits relatively stable performance under a wide range of humidity, the performance of the 3D flow field significantly outperforms that of conventional flow fields, with a minimum 40% improvement at different humidity conditions. Additionally, even in severe dry and wet conditions (4% RH and 150% RH), the 3D flow field demonstrates peak power densities of 1.40 W cm^{-2} and 1.49 W cm^{-2}, respectively, representing reductions of 18% and 12% compared to 60% RH. Notably, over the wide humidity range from 4% to 150%, the performance variation at 0.6 V is only 18%, outperforming the 25% fluctuation observed in commercial GDL. The 3D flow field still demonstrates considerable tolerance to a wide range of humidity, even under low air supply. At an air stoichiometric ratio of 1.5, the performance fluctuations are limited to an 8% range (Fig. S28†), while significant water flooding has already occurred in the conventional flow field at high humidity, leading to a decline in performance. Consequently, the excellent humidity tolerance of the 3D flow field will reduce the need for precise humidity control, thereby lowering parasitic power consumption and contributing to the more cost-effective PEMFCs system.[45]

The 3D flow field demonstrates remarkable mass transfer potential with moderate applied back pressure. Due to the increased reactant partial pressure and accelerated electrode reaction kinetics induced by back pressure,[46] the performance of both 3D and conventional flow fields is improved substantially as the back pressure increases from 0 kPa to 100 kPa (Fig. 4c and S29†). However, as the back pressure increases further to 150 kPa and 200 kPa, the performance tends to stabilize, which may be attributable to the increased membrane resistance, as previously reported.[47]

Outstandingly, the 3D flow field consistently outperforms the conventional flow field at all back pressures, as shown in Fig. 4d. Specifically, the power density at 0.6 V shows a 31% and 40% enhancement over the conventional flow field at 0 kPa and 100 kPa respectively, indicating its excellent mass transfer capability. Furthermore, the 3D flow field demonstrates superior high-performance potential under back pressure-assisted conditions. It demonstrates a greater performance improvement with 57% (from 0.97 W cm^{-2} to 1.53 W cm^{-2}) as the back pressure varies from 0 kPa to 100 kPa, while the conventional flow field increases by 47% (from 0.74 W cm^{-2} to 1.1 W cm^{-2}). Consequently, 100 kPa is identified as the optimal back pressure for the 3D flow field in PEMFCs, achieving high performance without the need for higher pressures, which will reduce the parasitic power consumption of air compressors and enhance overall energy efficiency.[48]

In addition, the constant current discharge process under 40 A (about 2.7 A cm^{-2}) of the 3D-patterned GDL for 100 h was

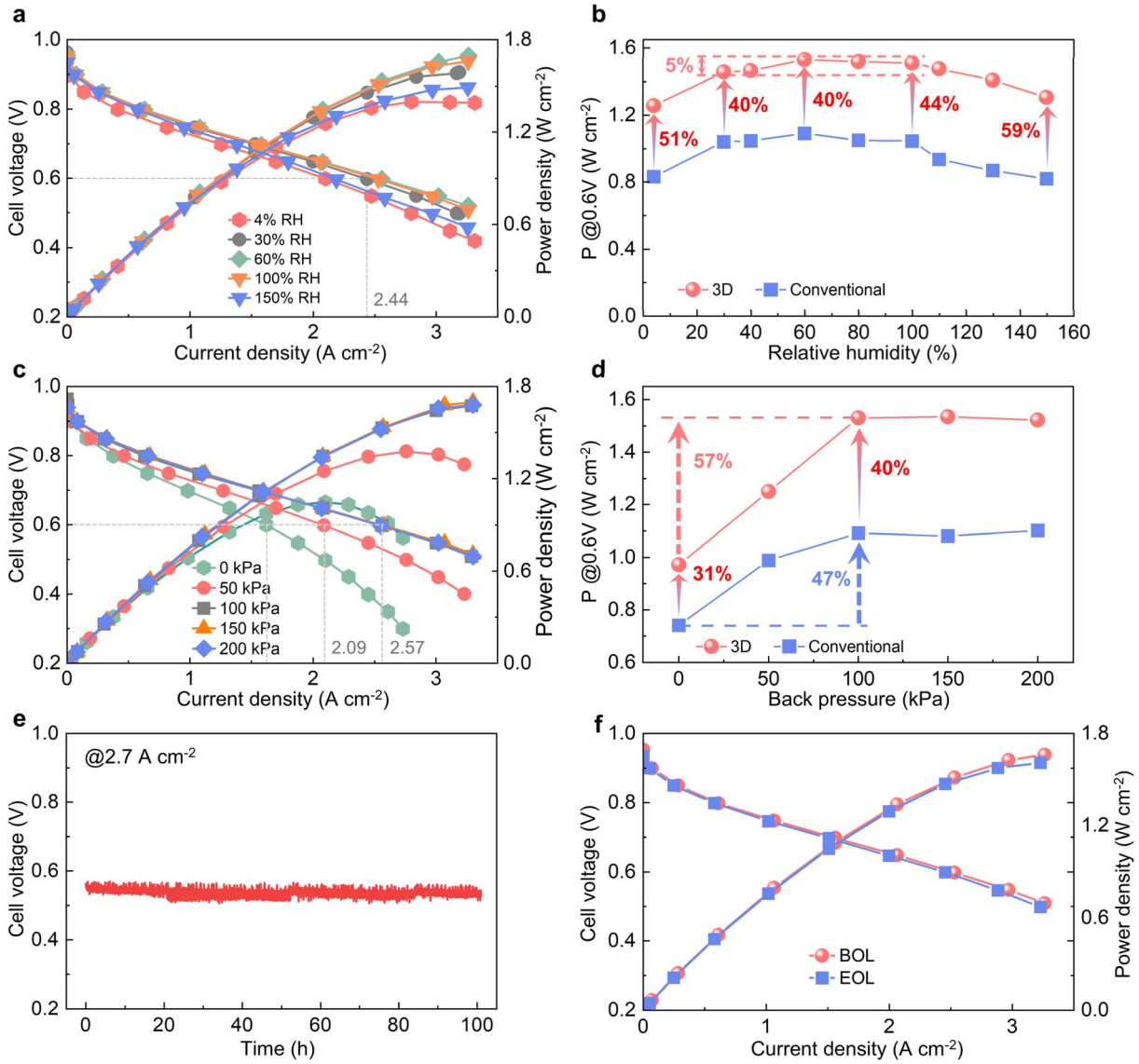

Fig. 4 Fuel cell performance and stability of the 3D flow field under different humidity and back pressure. (a) Polarization curves of the 3D flow field under different humidity levels (4% RH to 150% RH) at an air stoichiometric ratio of 2.5. The back pressure is maintained at 100 kPa. (b) Comparison of power density at 0.6 V under different humidity levels with an air stoichiometric ratio of 2.5. (c) Polarization curves of the 3D flow field under different back pressures at an air stoichiometric ratio of 2.5. The humidity is maintained at 60% RH. (d) Comparison of power density at 0.6 V under different back pressures with an air stoichiometric ratio of 2.5. (e) Stability test at 40 A (approximately 2.7 A cm^{-2}). (f) Polarization curves at the beginning of life (BOL) and end of life (EOL).

recorded and is shown in Fig. 4e. During the long-time discharge, the voltage fluctuates within the range of 0.566 V to 0.506 V, with an attenuation of roughly 10.6%. This further demonstrates that the 3D flow field exhibits robust water management ability, with negligible flooding under a high current density operation. The polarization curves before and after the long-term test are also compared (Fig. 4f). The peak power density decreases only slightly from 1.66 W cm^{-2} to 1.61 W cm^{-2}, with a reduction of merely 3%. These results exhibit excellent water drainage in the 3D flow field and minimal structural or compositional deterioration in the GDL after 100 h of continuous operation.

2.5 Mechanism analysis of the 3D flow field

An *ex situ* visualization experiment was designed to further investigate the water dynamic behavior in the 3D flow field. As shown in Fig. 5a and S31,† the visualization fixture comprises four components: a transparent acrylic end plate engraved with waveform flow channels in accordance with the flow field parameters in the bipolar plate used above, a PTFE gasket, the GDL, and a blank acrylic end plate with gasket. The 3D flow field is composed of the waveform flow channels on the end plate and the 3D patterns on the GDL. A volume of 50 μL liquid water was injected into the fixture through the inlet, and then a 120 mL min^{-1} airflow was continuously introduced to blow out the liquid water. A camera is positioned beside the end plate with

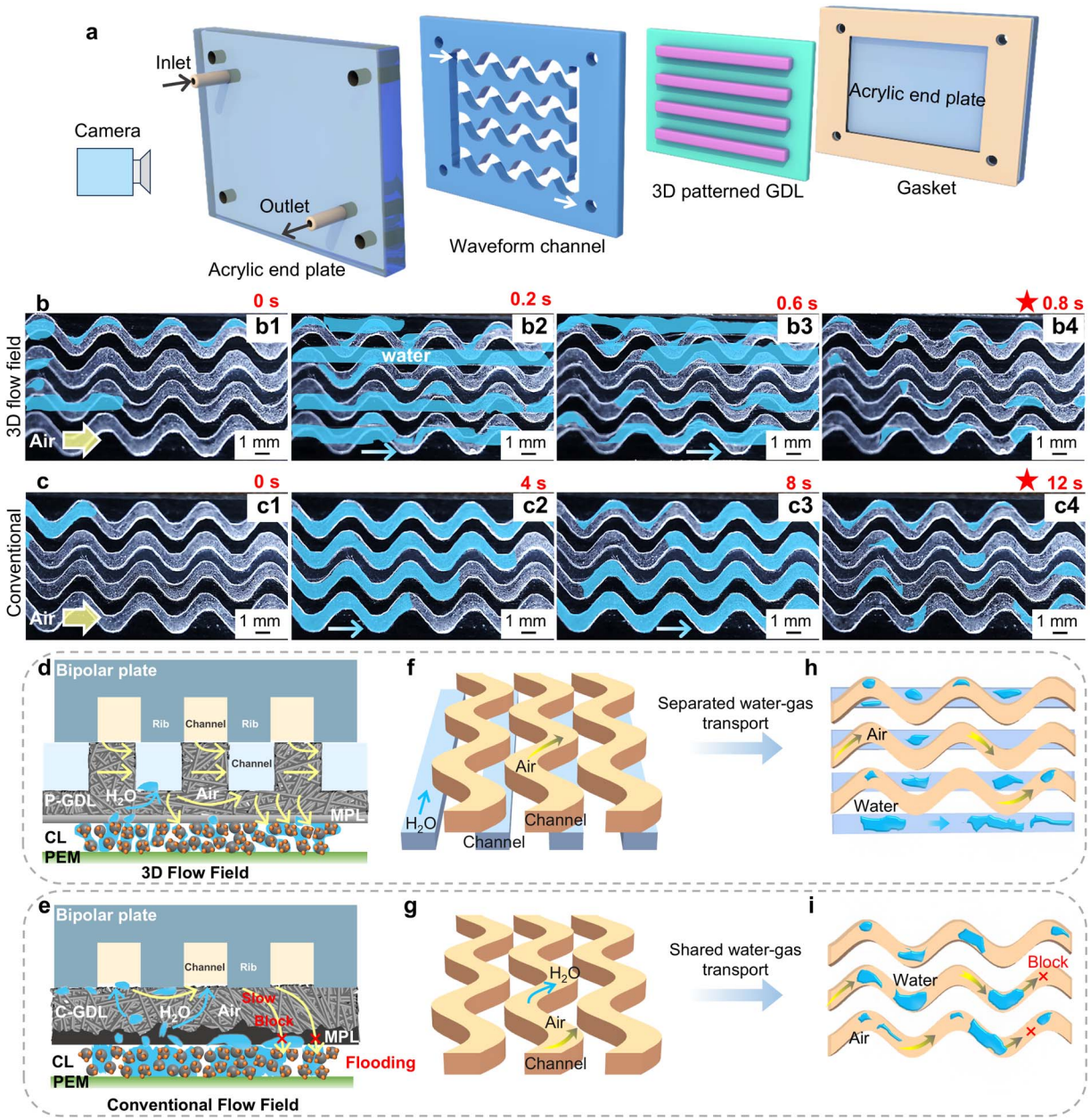

Fig. 5 Water management observation and mass transfer mechanism of the 3D flow field and conventional flow field. (a) Schematic of the water management observation method and fixture. (b) Optical pictures of the 3D flow field and (c) conventional flow field at different moments during observation. Cross-sectional schematic of the mass transfer mechanism in (d) the 3D flow field and (e) the conventional flow field. (f) Space of the 3D flow field structure. (g) Space of the conventional flow field structure. (h) Schematic of separated water-gas transport. (i) Schematic of shared water-gas transport.

flow channels to record the water flow in the 3D flow field, and the field of view is 0.8 cm × 3 cm. The moment when air began to flow was counted as 0 seconds.

The liquid water is completely expelled from the fixture in just 0.8 seconds (Video S1†). As shown in Fig. 5b, at 0 seconds, water (colored in blue) in the flow field begins to move towards the outlet under airflow (Fig. 5b1). By 0.2 seconds, a substantial portion of water has been swept away (Fig. 5b2). The main pathways of liquid water are the straight channels on the 3D-patterned GDL instead of the end plate on the wavy channels. Due to the narrow size and superhydrophobic nature of the straight channels on the 3D-patterned GDL, liquid water flows fast and has little resistance. By 0.6 seconds (Fig. 5b3), little water remains around the outlet, and by 0.8 seconds (Fig. 5b4), almost all injected water has been expelled. Because of the rough engraved surface, very little water remains in the wavy channels on the endplate.

In contrast, in a conventional flow field, water is removed at a much slower rate. It takes as long as 12 seconds for water drainage (Video S2† and Fig. 5c), which is 14 times longer than

the 0.8 seconds in the 3D flow field. There are two main reasons why liquid water flows slowly in the conventional flow field: the longer flow channels and weaker hydrophobicity. The wavy flow channels provide liquid water with longer non-linear pathways, leading to slower drainage. Also, the weaker hydrophobicity of flow channels on the endplate creates greater resistance to the flow of liquid water. Therefore, the *ex situ* experiment proves that the 3D flow field realizes a significantly higher drainage efficiency compared with the conventional flow field.

On the one hand, the enhanced mass transfer of the 3D flow field comes from the porous ribs on the 3D-patterned GDL. There is a more effective and sufficient oxygen supply to the catalyst layer. As shown in Fig. 5d, the porous ribs provide good gas permeability to achieve a uniform gas distribution and purge the excessive water beneath the solid ribs on the bipolar plate. However, the conventional flow field suffers from rib compression, which forms dead or low-velocity zones for airflow and causes water accumulation (Fig. 5e), thereby obstructing oxygen transport to the catalyst. Therefore, the 3D flow field overcomes the limitations of poor oxygen transport and water accumulation beneath the ribs of conventional bipolar plates, effectively mitigating concentration polarization in PEMFCs.

On the other hand, the 3D-patterned GDL creates exceptionally efficient water pathways, facilitating effective water discharge and enabling high current densities. Apart from the wavy channels provided by the bipolar plate, unique straight channels are created by the 3D-patterned GDL (Fig. 5f). Different from the simultaneous flow of air and water in the wavy channels (Fig. 5g), water follows independent pathways within the straight flow channels in a 3D flow field. As shown in Fig. 5h, excessive water passes through the MPL and support layer of the GDL into the straight flow channels, where it is rapidly expelled under airflow, with minimal water in the wavy channels. However, in the conventional flow channel, water and air share the wavy channels (Fig. 5i), resulting in a longer pathway for water removal due to the waveform structure, which increases the likelihood of water flooding. It will not only block oxygen pathways but also cover the active sites of catalysts, resulting in a substantial drop in the fuel cell performance. Therefore, the two distinct functional flow channels in the 3D flow field achieve water–gas separation successfully and ensure sufficient oxygen is delivered to the catalyst layer for reactions in PEMFCs.

3 Conclusions

We have reported a 3D flow field through an innovative, straightforward method, demonstrating exceptional PEMFC performance (peak power density of 1.7 W cm^{-2}) with a reduced pressure drop and substantial application potential. A porous, regularly 3D-patterned GDL is quickly obtained by vacuum filtration and integrated with a conventional bipolar plate to construct the 3D flow field structure. It features two distinct types of functional channels that effectively facilitate highly efficient water–gas separation and create shortcuts for rapid water removal. Moreover, despite retaining the conventional bipolar plate, the new design eliminates the dead or low-velocity zones typically formed by the ribs of bipolar plates. Owing to its excellent mass transfer and robust flooding resistance, the 3D flow field achieves a 73% performance improvement over conventional flow field at a low air stoichiometric ratio while maintaining stable fuel cell performance across a wide humidity range, with fluctuations limited to just 5%. Outperforming other reported new 3D flow field designs, our 3D flow field structure demonstrates considerable advantages through simplified manufacturing processes and reduced costs. The adjustability of 3D patterns through filtration molds, along with the retention of conventional bipolar plates, further enhances the broad applicability of the 3D flow field design strategy proposed here.

Data availability

All data supporting the findings of this study are available within the paper and its ESI.†

Author contributions

Xi Cheng designed the experiments, performed the data analysis, and drafted the manuscript. Can He, Qinglin Wen, Yuzhuo Jiang, and Wei Li assisted with the experiments, data analysis, and schematic drawing. Jiahao Huang, Wentao Huang, Xingyu Zhu, Li, and Xueyan Chu contributed experimental details and materials. Fandi Ning, Lining Sun, and Bin Tian provided suggestions for figures and writing analysis. Xiaochun Zhou supervised the project, suggested the experiments and data analysis, and revised the manuscript.

Conflicts of interest

There are no conflicts to declare.

Acknowledgements

The authors gratefully acknowledge the financial support from the National Natural Science Foundation of China (No. 22472198, 22172191) and CAS H2 Technology (Suzhou) Co., Ltd (E341150301). The authors also appreciate the technical support for SEM provided by Nano-X at the Suzhou Institute of Nano-Tech and Nano-Bionics (SINANO), Chinese Academy of Sciences.

References

1 N. Kittner, F. Lill and D. M. Kammen, *Nat. Energy*, 2017, **2**, 17125.
2 A. Rode, T. Carleton, M. Delgado, M. Greenstone, T. Houser, S. Hsiang, A. Hultgren, A. Jina, R. E. Kopp, K. E. McCusker, I. Nath, J. Rising and J. Yuan, *Nature*, 2021, **598**, 308–314.
3 M. McPherson, N. Johnson and M. Strubegger, *Appl. Energy*, 2018, **216**, 649–661.
4 P. Atanassov, *Joule*, 2018, **2**, 1210–1211.
5 R. Abbasi, B. P. Setzler and Y. Yan, *Energy Environ. Sci.*, 2023, **16**, 4404–4422.

6 M. Marappan, K. Palaniswamy, T. Velumani, K. B. Chul, R. Velayutham, P. Shivakumar and S. Sundaram, *Chem. Rec.*, 2021, **21**, 663–714.
7 K. Jiao, J. Xuan, Q. Du, Z. Bao, B. Xie, B. Wang, Y. Zhao, L. Fan, H. Wang, Z. Hou, S. Huo, N. P. Brandon, Y. Yin and M. D. Guiver, *Nature*, 2021, **595**, 361–369.
8 S. Jang, Y. S. Kang, D. Kim, S. Park, C. Seol, S. Lee, S. M. Kim and S. J. Yoo, *Adv. Mater.*, 2023, **35**, 2204902.
9 Y. Duan, H. Liu, W. Zhang, L. Khotseng, Q. Xu and H. Su, *J. Power Sources*, 2023, **555**, 232369.
10 G. Zhang, Z. Qu, W. Q. Tao, X. Wang, L. Wu, S. Wu, X. Xie, C. Tongsh, W. Huo, Z. Bao, K. Jiao and Y. Wang, *Chem. Rev.*, 2022, **123**, 989–1039.
11 M. B. Karimi, K. Hooshyari, P. Salarizadeh, H. Beydaghi, V. M. Ortiz-Martínez, A. Ortiz, I. Ortiz Uribe and F. Mohammadi, *Int. J. Hydrogen Energy*, 2021, **46**, 34413–34437.
12 F. Lapicque, M. Belhadj, C. Bonnet, J. Pauchet and Y. Thomas, *J. Power Sources*, 2016, **336**, 40–53.
13 N. Zamel and X. Li, *Prog. Energy Combust. Sci.*, 2013, **39**, 111–146.
14 C. A. Sarjuni, B. H. Lim, E. H. Majlan and M. I. Rosli, *Renewable Sustainable Energy Rev.*, 2024, **193**, 114292.
15 K. Tüber, A. Oedegaard, M. Hermann and C. Hebling, *J. Power Sources*, 2004, **131**, 175–181.
16 A. Iranzo, P. Boillat, J. Biesdorf, E. Tapia, A. Salva and J. Guerra, *Int. J. Hydrogen Energy*, 2014, **39**, 15687–15695.
17 A. Kazim, P. Forges and H. T. Liu, *Int. J. Energy Res.*, 2003, **27**, 401–414.
18 L. Yu, G. Ren, M. Qin and X. Jiang, *Renewable Energy*, 2009, **34**, 530–543.
19 M. Sauermoser, N. Kizilova, B. G. Pollet and S. Kjelstrup, *Front. Energy Res.*, 2020, **8**, 00013.
20 L. Xia, Z. Yu, G. Xu, S. Ji and B. Sun, *Energy Convers. Manage.*, 2021, **247**, 114707.
21 G. Cai, Y. Liang, Z. Liu and W. Liu, *Energy*, 2020, **192**, 116670.
22 H. Hu, X. Xu, N. Mei and G. Tong, *Ionics*, 2020, **26**, 6245–6253.
23 P. Xu, Q. Wen, S. Zou, H. Jin, Y. Li, W. Li, C. He, S. Pan, B. Tian, L. Yan, F. Ning and X. Zhou, *J. Mater. Chem. A*, 2023, **11**, 8845–8857.
24 Z. Qin, W. Huo, Z. Bao, C. Tongsh, B. Wang, Q. Du and K. Jiao, *Adv. Sci.*, 2022, **10**, 2205305.
25 H. Gu, C. Peng, Z. Qian, S. Lv, J. Feng, K. Luo, M. Zhan, P. Xu and X. Xu, *Int. J. Heat Mass Transfer*, 2024, **227**, 125543.
26 X. Chen, Z. Yu, C. Yang, Y. Chen, C. Jin, Y. Ding, W. Li and Z. Wan, *Int. J. Hydrogen Energy*, 2021, **46**, 11127–11139.
27 B. Wang, W. Chen, F. Pan, S. Wu, G. Zhang, J. W. Park, B. Xie, Y. Yin and K. Jiao, *J. Power Sources*, 2019, **434**, 226741.
28 N. Konno, S. Mizuno, H. Nakaji and Y. Ishikawa, *SAE International Journal of Alternative Powertrains*, 2015, **4**, 123–129.
29 Z. Bao, Z. Niu and K. Jiao, *J. Power Sources*, 2019, **438**, 226995.
30 H. Guo, L. Chen, S. A. Ismail, L. Jiang, S. Guo, J. Gu, X. Zhang, Y. Li, Y. Zhu, Z. Zhang and D. Han, *Materials*, 2022, **15**, 8800.
31 T. Kitahara, H. Nakajima, M. Inamoto and K. Shinto, *J. Power Sources*, 2014, **248**, 1256–1263.
32 M. Balakrishnan, P. Shrestha, N. Ge, C. Lee, K. F. Fahy, R. Zeis, V. P. Schulz, B. D. Hatton and A. Bazylak, *ACS Appl. Energy Mater.*, 2020, **3**, 2695–2707.
33 Q. Wen, S. Pan, Y. Li, C. Bai, M. Shen, H. Jin, F. Ning, X. Fu and X. Zhou, *ACS Energy Lett.*, 2022, **7**, 3900–3909.
34 D. Spernjak, R. Mukundan, R. L. Borup, L. G. Connolly, B. I. Zackin, V. De Andrade, M. Wojcik, D. Y. Parkinson, D. L. Jacobson, D. S. Hussey, K. L. More, T. Chan, A. Z. Weber and I. V. Zenyuk, *ACS Appl. Energy Mater.*, 2018, **1**, 6006–6017.
35 T. Li, K. Wang, J. Wang, Y. Liu, Y. Han, J. Song, H. Hu, G. Lin and Y. Liu, *J. Mater. Sci.*, 2020, **55**, 4558–4569.
36 W. Zhang, F. Guo, Y. Zhou, S. Yu, A. Chen, H. Jiang, H. Jiang and C. Li, *ACS Appl. Mater. Interfaces*, 2022, **14**, 17578–17584.
37 C. Csoklich, R. Steim, F. Marone, T. J. Schmidt and F. N. Büchi, *ACS Appl. Mater. Interfaces*, 2021, **13**, 9908–9918.
38 P. Lin, J. Sun, C. He, M. Wu and T. Zhao, *ACS Energy Lett.*, 2024, **9**, 1710–1716.
39 C. Csoklich, T. J. Schmidt and F. N. Büchi, *Energy Environ. Sci.*, 2022, **15**, 1293–1306.
40 X. Zhou, J. Zhang, K. Feng, Z. Qiao, Y. Wang and L. Shi, *J. Power Sources*, 2025, **626**, 235753.
41 S. Wan, H. Jiang, Z. Guo, C. He, X. Liang, N. Djilali and T. Zhao, *Energy Environ. Sci.*, 2022, **15**, 2874–2888.
42 W. Yang, R. Zhang, M. Lu, Y. Lin, L. Liang and Q. Xu, *Chem. Eng. J.*, 2024, **499**, 156346.
43 H. Chen, H. Guo, F. Ye and C. F. Ma, *J. Power Sources*, 2020, **472**, 228456.
44 C. He, Q. Wen, F. Ning, M. Shen, L. He, B. Tian, W. Li, L. Xu, Y. Liu, X. Dan, Z. Chai, S. Zou and X. Zhou, *Adv. Funct. Mater.*, 2024, **34**, 2302928.
45 H. Fu, J. Shen, L. Sun and K. Y. Lee, *Int. J. Hydrogen Energy*, 2021, **46**, 9905–9917.
46 J. Lu, G. Wei, F. Zhu, X. Yan and J. Zhang, *Fuel Cells*, 2019, **19**, 211–220.
47 J. Zhang, C. Song, J. Zhang, R. Baker and L. Zhang, *J. Electroanal. Chem.*, 2013, **688**, 130–136.
48 D. K. Kim, J. S. Koh, M. S. Kim and H. H. Song, *Int. J. Hydrogen Energy*, 2015, **40**, 12370–12381.

